

Validation of Particle-Laden Large-Eddy Simulation using HPC Systems

Konstantin Fröhlich, Lennart Schneiders, Matthias Meinke and Wolfgang Schröder

Abstract In this contribution, results of a direct particle-fluid simulation (DPFS) are compared with direct numerical simulations and large-eddy simulations (LES) using a popular Euler-Lagrange method (ELM). DPFS facilitates the computation of particulate turbulent flow with particle sizes on the order of the smallest flow scales, which requires advanced numerical methods and parallelization strategies accompanied by considerable computing resources. After recapitulating methods required for DPFS, a setup is proposed where DPFS is used as a benchmark for direct numerical simulations and LES. Therefore, a modified implicit LES scheme is proposed, which shows convincing statistics in comparison to a direct numerical simulation of a single phase flow. Preliminary results of particle-laden flow show good agreement of the LES and the DPFS findings. Further benchmark cases for an appreciable range of parameters are required to draw a rigorous conclusion of the accuracy of the ELM.

K. Fröhlich · L. Schneiders · M. Meinke
Institute of Aerodynamics, RWTH Aachen University, Aachen, Germany,
e-mail: k.froehlich@aia.rwth-aachen.de

L. Schneiders
e-mail: l.schneiders@aia.rwth-aachen.de

M. Meinke
e-mail: m.meinke@aia.rwth-aachen.de

W. Schröder
Institute of Aerodynamics, RWTH Aachen University, Aachen, Germany
Jülich Aachen Research Alliance - High Performance Computing
e-mail: office@aia.rwth-aachen.de

1 Introduction

Particle-laden turbulent flow is of importance in a broad field of applications including natural and technical environments. Examples may be found in the settling of aerosol particles in atmospheric flows, in the transport of dust through the human respiration system, in fuel injections of internal combustion engines, as well as in the combustion of pulverized coal particles in a furnace. However, for particles with diameter $d_p \approx \eta_k$, with η_k the Kolmogorov scale, there is no accurate and robust model available [1]. This may be explained by the numerous scales involved, since an accurate computation of particle-laden flow requires the full resolution of the flow up to the sub-Kolmogorov scale. Only recently, access has been gained to direct particle-fluid simulations (DPFS), where all relevant scales are fully resolved without employing any models [15]. Fundamental studies have been performed and the modulation of isotropic turbulence by particles has been investigated [18], [19], which provide now a sound basis for the development of models suitable for industrial applications. A first simplification of DPFS is the direct numerical simulation (DNS), where all turbulent scales are resolved, while the particle-fluid interaction is modeled by an Euler-Lagrange model (ELM). However, DNS still requires considerable computational resources. A further simplification is provided by large-eddy simulations (LES), where large energy containing scales are resolved while models for small subgrid scales are employed mainly responsible for the dissipation.

In this contribution, a setup is developed for the comparison of DPFS, DNS, and LES, offering the possibility to use the insights gained in [18] and [19] for the development of ELM models in the framework of LES. After presenting the governing equations in Sec. 2, the numerical methods developed for the DPFS are briefly recapitulated, and an implicit LES model is introduced in Sec. 3. In Sec. 4 the latter is validated for single phase flow, and subsequently, statistics generated by LES and DNS are compared with the results of DPFS. Section 5 gives a brief conclusion emphasizing the need of further benchmark cases for a thorough analysis of the differences between the results of LES, DNS, and DPFS.

2 Mathematical Models

In this section, mathematical models are introduced which are capable of describing the motion of small particles suspended in a flow field. The mathematical model of the fluid phase will be given in Sec. 2.1. Thereafter, the motion of particles will be described by model equations for DPFS fulfilling the no-slip condition at particle surfaces as well as using a popular Lagrangian point particle approach in Sec. 2.2.

2.1 Navier-Stokes Equations

The conservation of mass, momentum, and energy in a time-dependent control volume V with the surface ∂V moving with the velocity $\mathbf{u}_{\partial V}$ may be expressed in integral form by

$$\int_{V(t)} \frac{\partial \mathbf{Q}}{\partial t} dV + \int_{\partial V(t)} \bar{\mathbf{H}} \cdot \mathbf{n} dA = \mathbf{0}, \quad (1)$$

where $\mathbf{Q} = [\rho_f, \rho_f \mathbf{u}^T, \rho_f E]^T$ is the vector of conservative Eulerian variables and $\bar{\mathbf{H}}$ is the flux tensor through ∂V in outward normal direction \mathbf{n} . The conservative variables are defined by the fluid density ρ_f , the vector of velocities \mathbf{u} , and the total specific energy $E = e + |\mathbf{u}|^2/2$ containing the specific internal energy e . It is physically meaningful as well as useful for the development of numerical schemes to divide $\bar{\mathbf{H}}$ into an inviscid part $\bar{\mathbf{H}}_{\text{inv}}$ and a viscous part $\bar{\mathbf{H}}_{\text{visc}}$, where

$$\bar{\mathbf{H}} = \bar{\mathbf{H}}_{\text{inv}} + \bar{\mathbf{H}}_{\text{visc}} = \begin{pmatrix} \rho_f \mathbf{u} \\ \rho_f \mathbf{u} (\mathbf{u} - \mathbf{u}_{\partial V}) + p \bar{\mathbf{I}} \\ \rho_f E (\mathbf{u} - \mathbf{u}_{\partial V}) + \mathbf{u} p \bar{\mathbf{I}} \end{pmatrix} - \frac{1}{Re} \begin{pmatrix} \mathbf{0} \\ \bar{\boldsymbol{\tau}} \\ \bar{\boldsymbol{\tau}} \mathbf{u} - \mathbf{q} \end{pmatrix}, \quad (2)$$

with the pressure p , the stress tensor $\bar{\boldsymbol{\tau}}$, the vector of heat conduction \mathbf{q} , the unit tensor $\bar{\mathbf{I}}$, and the Reynolds number Re . The latter is determined by $Re = \frac{\rho_{\infty} u_{\infty} L}{\mu_{\infty}}$, given the reference quantities of the density ρ_{∞} , the velocity u_{∞} , the length L_{∞} , and the dynamic viscosity μ_{∞} . Using Stokes' hypothesis for a Newtonian fluid yields an equation for the stress tensor

$$\bar{\boldsymbol{\tau}} = 2\mu \bar{\mathbf{S}} - \frac{2}{3}\mu (\nabla \cdot \mathbf{u}) \bar{\mathbf{I}}, \quad (3)$$

in which $\bar{\mathbf{S}}$ holds the rate-of-strain tensor defined as $\bar{\mathbf{S}} = \frac{(\nabla \mathbf{u} + (\nabla \mathbf{u})^T)}{2}$. The dynamic viscosity μ depends on the local thermodynamic state of the fluid. However, it can be approximately obtained by Sutherland's law

$$\mu(T) = \mu_{\infty} \left(\frac{T}{T_{\infty}} \right)^{3/2} \frac{T_{\infty} + S}{T + S}, \quad (4)$$

with S being the Sutherland temperature. Fourier's law gives the heat conduction

$$\mathbf{q} = -\frac{\mu}{Pr(\gamma - 1)} \nabla T, \quad (5)$$

using the static temperature T , the constant capacity ratio $\gamma = c_p/c_v$, the specific heat capacities c_v and c_p at constant volume and at constant pressure. The Prandtl number Pr is given by $Pr = \frac{\mu_{\infty} c_p}{k_t}$ containing the thermal conductivity k_t . The system of equations can be closed by the caloric state equation $e = c_v T$ and the state equation of an ideal gas $p = \rho R T$, with R being the specific gas constant.

2.2 Particle Dynamics

In this contribution, dilute suspensions of small, rigid, spherical particles with statistically negligible collisions are investigated. The volume fraction $\Phi_p = V_p/V$, with the volume occupied by particles V_p and the overall volume V , is small, i.e., $\Phi_p \ll 1$, while the mass fraction $\psi_p = M_p/m_f$, with the overall mass of particles M_p and the mass of the fluid m_f , has a finite value, which yields an interaction between inertial particles and the smallest turbulent scales referred to as two-way coupling [4]. The linear motion of a particle p with the velocity \mathbf{v}_p and mass m_p at the position \mathbf{x}_p is given by the relations

$$\frac{d\mathbf{x}_p}{dt} = \mathbf{v}_p, \quad (6)$$

$$m_p \frac{d\mathbf{v}_p}{dt} = \mathbf{F}. \quad (7)$$

The rotational movement $\boldsymbol{\omega}_p$ of the particles may be described conveniently in a rotating frame of reference $(\tilde{x}, \tilde{y}, \tilde{z})$, which is aligned with the principal components of the particles and fixed at its center of mass, with the equation

$$\tilde{\mathbf{I}} \frac{d\tilde{\boldsymbol{\omega}}_p}{dt} + \tilde{\boldsymbol{\omega}}_p \times (\tilde{\mathbf{I}} \tilde{\boldsymbol{\omega}}_p) = \tilde{\mathbf{T}}, \quad (8)$$

where $\tilde{\mathbf{I}}$ denotes the principal moments of inertia. The particle dynamics can be fully described, provided that the hydrodynamic force \mathbf{F} and torque \mathbf{T} acting on the particle are known. These are differently determined by DPFS and ELM, as pointed out in the following.

Direct Particle-Fluid Simulation

The full resolution of the particles establishes the no-slip condition at particle surface Γ_p , i.e., the fluid velocity on the particle surface with the particle radius \mathbf{r}_p is given by

$$\mathbf{u} = \mathbf{v}_p + \boldsymbol{\omega}_p \times (\mathbf{x}_p - \mathbf{r}_p). \quad (9)$$

Therefore, the hydrodynamic force and torque is defined by the surface integrals

$$\mathbf{F}_p = \oint_{\Gamma_p} (-p\mathbf{n} + \bar{\boldsymbol{\tau}} \cdot \mathbf{n}) dA \quad (10)$$

$$\mathbf{T}_p = \oint_{\Gamma_p} (\mathbf{x} - \mathbf{r}_p) \times (-p\mathbf{n} + \bar{\boldsymbol{\tau}} \cdot \mathbf{n}) dA. \quad (11)$$

It should be noted that the impact of the particles on the fluid is naturally given without employing any models in contrast to ELM.

Euler-Lagrange Model

For the ELM, the no-slip condition cannot be imposed and the hydrodynamic force acting on the particles has to be modeled. Therefore, a popular simplification (e.g. [1]) of the semi-empirical Maxey-Riley equation [9], with

$$\mathbf{F}_{pp} = 3\pi\mu d_p(\mathbf{u} - \mathbf{v})\phi(Re_p), \quad (12)$$

is used in this contribution, which represents the quasi-steady Stokes drag with an empirical correction function $\phi(Re_p)$ containing the particle Reynolds number Re_p . However, the validity of Eq. (12) is essentially limited by the constraint $d_p/\eta_k \ll 1$. Specifically, with $\eta_k \sim l_0 Re^{-3/4}$ and l_0 as the length scale of the largest eddy, Eq. (12) has only restricted significance for industrial and natural flow conditions which have in general a high Re . Additionally, the coupling force \mathbf{F}_{pp} has to be included in the momentum balance of Eq. (1) to establish the interphase coupling. Equations (1) and (12) yield a closed system of equations together with the equations of linear motion, provided that the undisturbed fluid velocity at the particle position \mathbf{x}_p may be estimated by interpolation of the disturbed fluid velocity at the particle position using the Eulerian velocities of the carrier flow. However, this estimate is only valid for $d_p \ll \Delta$ [3], with Δ the grid width, which again limits the applicability of the ELM. The hydrodynamic torque is negligible for small spherical particles and may thus be safely omitted.

3 Numerical Methods

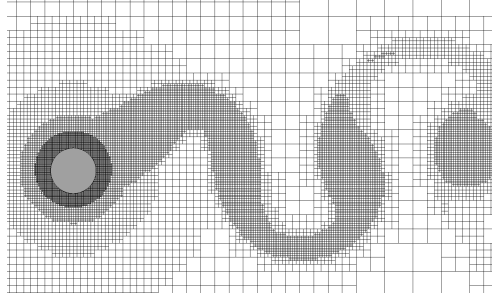
In this section, numerical methods for the solution of the system of equations given in Sec. 2 will be presented. First, methods for DPFS presented in [16], [13], and [15] will be briefly described. Next, an implicit LES will be introduced, which allows to control the amount of numerical dissipation added by the numerical schemes. This section will be closed with the solution schemes necessary for the ELM.

DPFS as well as the implicit LES rely on a cell-centered finite-volume formulation employing Cartesian meshes. A highly scalable efficient parallel mesh generator is available [7], where the domain decomposition is based on a weighted Hilbert curve. The inviscid fluxes $\bar{\mathbf{H}}_{inv}$ are computed by a variant of the AUSM [8] with a modified pressure splitting proposed in [11]. Second-order accuracy is achieved via a MUSCL extrapolation routine [23], while the extrapolation uses the cell-centered gradients of the primitive variables obtained by a weighted second-order least-squares approach [15]. The viscous fluxes $\bar{\mathbf{H}}_{visc}$ are computed by a recentering approach proposed in [2].

3.1 Direct Particle-Fluid Simulation

DPFS relies on an accurate computation of freely moving boundaries. This is achieved via a level-set function for the sharp representation of the boundaries and a strictly conservative numerical discretization of the cut cells at the boundaries. Using multiple level-set functions allows the resolution of particle collisions [14]. Instabilities due to arbitrary small cut cells are suppressed by an accurate interpolation scheme and conservation is ensured by a flux-redistribution technique, which also handles emerging and submerging cells due to the moving boundaries [15]. Several strategies are employed to mitigate the computational effort. First, a novel predictor-corrector Runge-Kutta scheme has been developed, which substantially reduces the overhead of remeshing and reinitialization of the solver due to the moving boundaries [15]. Next, a solution-adaptive refinement strategy generates automatically the mesh used during the solution of the flow field (cf. Fig. 1). Hence, the mesh is constantly changing since the particle positions and the flow field are different after each time step, which yields a significant load imbalance. Therefore, a dynamic load bal-

Fig. 1 Adaptively refined grid for an elastically mounted sphere. Distances to boundaries as well as sensors for entropy gradients and vorticity control the refinement. For details on the flow case, the reader is referred to [17], while the adaptive mesh refinement is described in [6].



ancing method has been developed to allow the use of high-performance computers for the solution of particle-laden flows. After a predefined number of time steps, a Hilbert curve is computed on the coarsest refinement level and weighted by the number of offsprings of each cell. This yields a unique balanced domain decomposition, which can be used to redistribute the cells among the processes. Since the domain boundaries are shifted moderately, only a part of the cells in the domains have to be exchanged. Figure 2 shows a comparison of the performance for a static and dynamic domain decomposition, which has been measured for $\mathcal{O}(1000)$ particles suspended in a Taylor-Green vortex [13]. A DPFS would eventually run out of memory on a static domain decomposition, whereas a dynamic domain decomposition yields an almost constant mean wall time. The overhead for the additional communication of 6% is small compared to the speed-up gained by load-balancing.

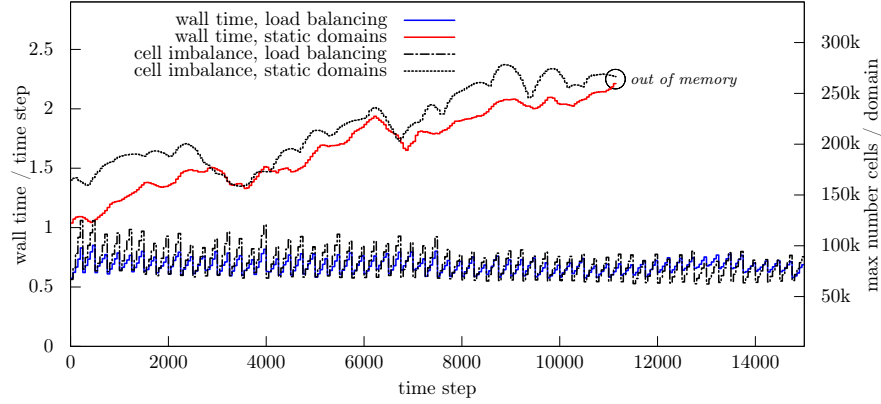


Fig. 2 Comparison of the performance of the static and dynamic loadbalancing. Due to the preferential concentration of the particle, the load imbalance grows, and eventually exceeds the available memory, if a static domain decomposition is used. A dynamic domain decomposition yields a sawtooth-curve, where the load balancing has been performed every 250th time step.

3.2 Implicit Large-Eddy Simulation

An AUSM scheme with a modified pressure splitting is available and it has been already shown that it is suited as an implicit LES scheme [11]. To reduce the dissipative behavior of the second-order discretization in low-Mach number flows, a modified version of the reconstruction method proposed in [22] is used. This reconstruction method alters the extrapolated velocities $u_{L/R}$ at the cell faces which are needed for the AUSM by

$$\begin{aligned} u_L^* &= \frac{u_L + u_R}{2} + z \frac{u_L - u_R}{2}, \\ u_R^* &= \frac{u_L + u_R}{2} + z \frac{u_R - u_L}{2}, \end{aligned} \quad (13)$$

where $u_{L/R}^*$ are the altered surface velocities and $z \leq 1$ may be in general an arbitrary function. It will be chosen

$$z = \min(1, \lambda \max(M_r^n, M_l^n)), \quad (14)$$

with the normal Mach numbers $M_{r,l}^n$ at the cell surfaces and λ as a grid resolution dependent constant. A value of $z = 1$ recovers the original MUSCL scheme, whereas for z tending to zero the surface velocities are obtained by central differencing such that velocity jumps are smoothed in low Mach number flows. The viscous fluxes are computed using a low-dissipation variation of the central scheme proposed in [2], where the normal derivatives of the normal velocity component will be computed at a surface of a cell i using a mixed five- and three-point stencil

$$\left(\frac{\partial u}{\partial x}\right)_{i+1/2} \approx \kappa \frac{u_{i+1} - u_i}{\delta x} + (1 - \kappa) \frac{\left(\frac{\partial u}{\partial x}\right)_i + \left(\frac{\partial u}{\partial x}\right)_{i+1}}{2}, \quad (15)$$

where κ is again a grid resolution dependent constant, δx is the grid spacing, and x only serves as an auxiliary coordinate direction. All other derivatives are computed via the five-point stencil as proposed by [2]. The implicit LES model is validated against a DNS of a single-phase isotropic turbulent flow in Sec. 4.1.

3.3 Euler-Lagrange Model

In the ELM, the particles are tracked solving the Eqs. (6), (7), and (12) by a predictor-corrector scheme described in [21]. In dilute suspensions particle collisions are statistically irrelevant and thus neglected. In general, particle positions do not coincide with the cell centers and the velocity of the carrier flow "seen" by the particles has to be interpolated. Ordinary interpolation routines, however, introduce filtering errors leading to a systematic underestimate of the turbulent kinetic energy after interpolation. To avoid filtering effects, the nearest cell-centered velocity is used instead of an interpolation routine.

As described in Sec. 2, the coupling of the force in Eq. (12) has to be projected onto the grid to establish a two-way coupling. Therefore, the force is smoothly projected using the distance based weighting function

$$\mathbf{F}_{\text{proj},i} = \mathbf{F}_{\text{pp}} \cdot \frac{e^{-(d_i^2/(\sigma\Delta^2))}}{\sum_i e^{-(d_i^2/(\sigma\Delta^2))}} \quad (16)$$

onto the nearest cells, with $\mathbf{F}_{\text{proj},i}$ the force projected on the cell i , d_i^2/Δ^2 the normalized distance between the cell center of the cell i and the particle center, and σ a smoothing parameter. The quantity σ is chosen sufficiently high to avoid self-induced disturbances [10].

4 Results and Discussion

Isotropic particle-laden flow is examined using the numerical methods presented in Sec. 3 to solve the equations introduced in Sec. 2. The flow field of a fully periodic cube with an edge length of L is initialized randomly and divergence free while fulfilling the realizability conditions [20]. To avoid compressibility effects, the Mach number was set to 0.1. The initialization procedure follows the method proposed in [12], where a prescribed energy spectrum $E(k)$ serves as initial condition with the model spectrum

$$E(k) = \left(\frac{3u_0^2}{2} \right) \left(\frac{k}{k_p} \right)^2 \exp \left(-\frac{k}{k_p} \right), \quad (17)$$

the wave number $k = |\mathbf{k}|$ including the wave number vector \mathbf{k} , the peak wave number k_p , and the initial dimensionless root-mean square velocity (rms-velocity) u_0 . The peak wave number is chosen $k_p = 4k_0$ with $k_0 = 2\pi/L$. The pressure field is computed by solving the Poisson equation in spectral space as shown in [20] and the density field is obtained assuming an isothermal flow field. The initial microscale Reynolds number is set to $Re_{\lambda 0} = 79.1$. For the initialization of the LES, the energy spectrum is cut off at the highest resolvable wave number.

In the following, it will be shown that the LES is capable of predicting the single-phase isotropic turbulence correctly. Subsequently, a particle-laden case is examined and DNS as well as LES using the ELM are compared with DPFS.

4.1 Large-Eddy Simulation of Isotropic Turbulence

Three grid resolutions with 64^3 , 96^3 , and 128^3 cells have been used for the LES. The findings have been compared with the results of a DNS with 256^3 cells. Figure 3 shows the temporal development of turbulent kinetic energy using an LES with 64^3 cells for different parameters λ in comparison to a DNS using 256^3 , and to the original AUSM-scheme without a modification of the extrapolated velocities. In this contribution, the turbulent kinetic energy E_k is normalized by its initial value $E_{k,0}$, whereas the time t is normalized by the initial eddy turnover time, i.e., $t^* = t\varepsilon_0/u_0^2$, with the initial viscous dissipation rate ε_0 . It can be observed that the original AUSM-scheme suffers substantially from an enhanced numerical dissipation, which can not be used as an implicit turbulence model for this flow regime. The modification offers a remedy and improves the results significantly for any parameter λ . Choosing the optimal parameters for λ and κ yields results matching the DNS for all resolutions as can be seen in Fig. 4.

4.2 Turbulence Modulation by Particles

Next, the particles are induced randomly into the turbulent flow at $t_i^* = 0.27$, which allows the turbulent flow to establish a non-linear turbulent transport (e.g. [5]). 45,000 particles with a particle density ratio $\rho_p/\rho_f = 1000$ and diameter on the order on the initial Kolmogorov scale, i.e., $d_p/\eta_k = 1.32$, are initialized with the local fluid velocity. The results of the DNS and the LES using the ELM proposed in Sec. 3.3 are validated against the benchmark results of a DPFS analyzed in [18]. An instantaneous snapshot of the flow field of a DPFS is shown in Fig. 5. Note that DPFS strongly relies on high performance computing systems, i.e., the DPFS per-

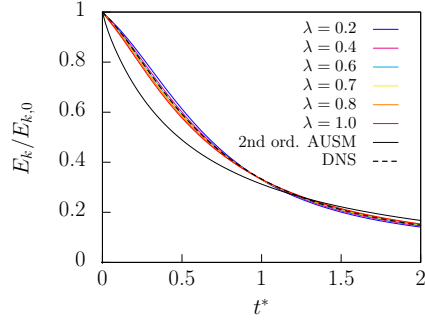


Fig. 3 Turbulent kinetic energy using LES with the modification according to Eq. 3.2 in comparison to the original AUSM scheme and a DNS

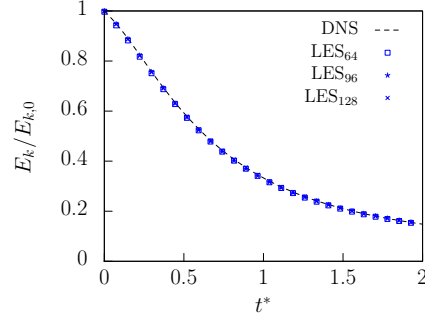
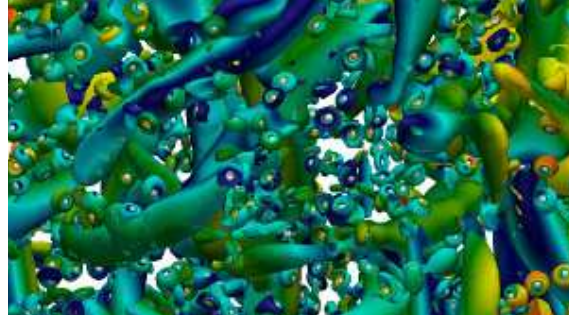


Fig. 4 Turbulent kinetic energy using LES with the optimal parameter combination λ and κ for three grid resolutions

formed in [18] required 48,000 computing cores on the Cray XC 40 of the HLRS. Moreover, the simulations using adaptive mesh refinement required about $2 \cdot 10^9$ cells, while a uniform mesh would require about $68 \cdot 10^9$ cells to resolve the flow field in the vicinity of the particles with the same accuracy.

Figure 6 and 7 show a comparison of a DNS and an LES using ELM with the DPFS.

Fig. 5 Instantaneous snapshot of the parallel projection of the turbulent particle-laden flow field. The structures are contours of the λ_2 criterion, whereas the color represents the velocity magnitude. Large vortical structures as well as particle induced structures in the vicinity of the particles are observed.



In Fig. 6 it can be seen that the particles attenuate the turbulent kinetic energy moderately, which is correctly predicted by the ELM independent from the resolution. Correspondingly, Fig. 7 shows the mean kinetic energy of the particles $K(t)$ normalized by the initial turbulent kinetic energy. A slight difference increasing moderately with time may be observed between the DPFS and the ELM, where the ELM is independent from the resolution. However, these preliminary results represent only a first validation of the ELM and further analyses are required to verify its reliability and robustness.

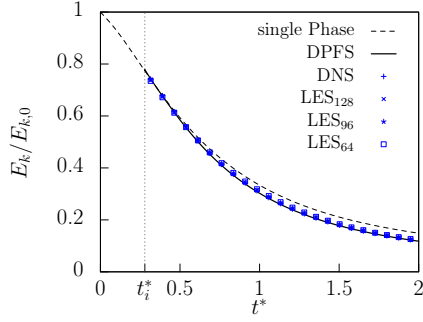


Fig. 6 Turbulent kinetic energy of particle-laden isotropic turbulence using DPFS in comparison to DNS and LES using the ELM

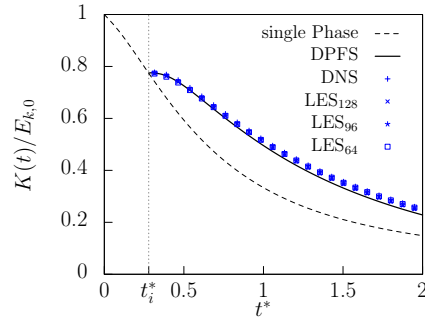


Fig. 7 Mean kinetic energy of the particles in DPFS in comparison to LES and DNS using the ELM

5 Conclusion

A setup has been presented for the validation of LES and DNS using an ELM model against benchmark results generated via DPFS. Therefore, an implicit LES formulation is employed which facilitates the use of ELM for different grid resolutions. Preliminary results show only slight deviations between the DPFS and the ELM for all grid resolutions. However, this behavior is certainly dependent on various parameters. Therefore, the validation of the ELM requires more benchmark cases using DPFS. In particular, it is planned to study the turbulence modulation by larger spherical particles, non-spherical particles, and non-isothermal particles.

Acknowledgements This work has been funded by the German Research Foundation (DFG) within the framework of the SFB/Transregio 129 "Oxyflame" (subproject B2). The support is gratefully acknowledged. Computing resources were provided by the High Performance Computing Center Stuttgart and by the Jülich Supercomputing Center (JSC) within a Large-Scale Project of the Gauss Center for Supercomputing (GCS).

References

1. Balachandar, S., Eaton, J. K.: Turbulent dispersed multiphase flow. *Annu. Rev. Fluid Mech.* **42**, 111–133 (2010).
2. Berger, M., Aftosmis, M.: Progress towards a Cartesian cut-cell method for viscous compressible flow. *AIAA Paper 2012-1301*, (2012).
3. Boivin, M., Simonin, O., Squires, K. D.: Direct numerical simulation of turbulence modulation by particles in isotropic turbulence. *J. Fluid Mech.* **375**, 235–263 (1998).
4. Elghobashi, S.: On predicting particle-laden turbulent flows. *Appl. Sci. Res.* **52**, 309–329 (1994).

5. Elghobashi, S., Truesdell, G.: On the two-way interaction between homogeneous turbulence and dispersed solid particles. I: Turbulence modification. *Phys. Fluids A* **5**, 1790–1801 (1993).
6. Hartmann, D., Meinke, M., Schröder, W.: An adaptive multilevel multigrid formulation for Cartesian hierarchical grid methods. *Comp. Fluids* **37**, 1103–1125 (2008).
7. Lintermann, A., Schlimpert, S., Grimmer, J., Günther, C., Meinke, M., Schröder, W.: Massively parallel grid generation on HPC systems. *Comput. Methods in Appl. Mech. Eng.* **277**, 131–153 (2014).
8. Liou, M.-S., Steffen, C. J.: A new flux splitting scheme. *J. Comput. Phys.* **107**, 23–39 (1993).
9. Maxey, M. R., Riley, J. J.: Equation of motion for a small rigid sphere in a nonuniform flow. *Phys. Fluids* **26**, 883–889 (1983).
10. Maxey, M., Patel, B., Chang, E., Wang, L.-P.: Simulations of dispersed turbulent multiphase flow. *Fluid Dyn. Res.* **20**, 143–156 (1997).
11. Meinke, M., Schröder, W., Krause, E., Rister, T.: A comparison of second- and sixth-order methods for large-eddy simulations. *Comput. Fluids* **31**, 695–718 (2002).
12. Orszag, S. A.: Numerical methods for the simulation of turbulence. *Phys. Fluids* **12**, II–250 (1969).
13. Schneiders, L., Grimmer, J. H., Meinke, M., Schröder, W.: An efficient numerical method for fully-resolved particle simulations on high-performance computers. *PAMM* **15**, 495–496 (2015).
14. Schneiders, L., Günther, C., Grimmer, J. H., Meinke, M. H., Schröder, W.: Sharp resolution of complex moving geometries using a multi-cut-cell viscous flow solver. *AIAA* 2015-3427, (2015).
15. Schneiders, L., Günther, C., Meinke, M., Schröder, W.: An efficient conservative cut-cell method for rigid bodies interacting with viscous compressible flows. *J. Comput. Phys.* **311**, 62–86 (2016).
16. Schneiders, L., Hartmann, D., Meinke, M., Schröder, W.: An accurate moving boundary formulation in cut-cell methods. *J. Comput. Phys.* **235**, 786–809 (2013).
17. Schneiders, L., Meinke, M., Schröder, W.: A robust cut-cell method for fluid-structure interaction on adaptive meshes. *AIAA Paper* 2013-2716, (2013).
18. Schneiders, L., Meinke, M., Schröder, W.: Direct particle-fluid simulation of Kolmogorov-length-scale size particles in decaying isotropic turbulence. *J. Fluid Mech.* **819**, 188–227 (2017).
19. Schneiders, L., Meinke, M., Schröder, W.: On the accuracy of Lagrangian point-mass models for heavy non-spherical particles in isotropic turbulence. *Fuel* **201**, 2–14 (2017).
20. Schumann, U., Patterson, G.: Numerical study of pressure and velocity fluctuations in nearly isotropic turbulence. *J. Fluid Mech.* **88**, 685–709 (1978).
21. Siewert, C., Kunnen, R., Schröder, W.: Collision rates of small ellipsoids settling in turbulence. *J. Fluid Mech.* **758**, 686–701 (2014).

22. Thornber, B., Mosedale, A., Drikakis, D., Youngs, D., Williams, R. J.: An improved reconstruction method for compressible flows with low Mach number features. *J. Comput. Phys.* **227**, 4873–4894 (2008).
23. Van Leer, B.: Towards the ultimate conservative difference scheme. V. A second-order sequel to Godunov’s method. *J. Comput. Phys.* **32**, 101–136 (1979).